

Combined deformation and solidification driven porosity formation in Aluminium alloys

S. Bhagavath^{1,2}, B. Cai³, R. Atwood⁴, M. Li⁵, B. Ghaffari⁵, P.D. Lee^{2,6+}, S. Karagadde¹⁺

¹Department of Mechanical Engineering, Indian Institute of Technology Bombay, Mumbai
400076, India

²Research Complex at Harwell, Harwell Campus, OX11 0FA UK,

³School of Metallurgy and Materials, University of Birmingham, Edgbaston, Birmingham,
B15 2TT UK,

⁴Diamond Light Source, Harwell Campus, OX11 0DE, UK

⁵Ford Research and Advanced Engineering, Dearborn, USA

⁶University college of London, London WC1E 6BT, UK

⁺ Corresponding authors: s.karagadde@iitb.ac.in, peter.lee@ucl.ac.uk

Abstract

In die-casting processes, the high cooling rates and pressures affect the alloy solidification and deformation behaviour, and thereby impact the final mechanical properties of cast components. In this study, isothermal semi-solid compression and subsequent cooling of aluminium die-cast alloy specimens were characterised using fast synchrotron tomography. This enabled the investigation and quantification of gas and shrinkage porosity evolution during deformation and solidification. The analysis of the 4D images (3D plus time) revealed two distinct mechanisms by which porosity formed; (i) deformation-induced growth due to the enrichment of local hydrogen content by the advective hydrogen transport, as well as a pressure drop in the dilatant shear bands, and (ii) diffusion-controlled growth during the solidification. The rates of pore growth were quantified throughout the process, and a Gaussian distribution function was found to represent the variation in the pore growth rate in both regimes. Using a one-dimensional diffusion model for hydrogen pore growth, the hydrogen flux required for driving pore growth during these regimes was estimated, providing a new insight into the role of advective transport associated with the deformation in the mushy region.

Keywords: die casting; gas and shrinkage porosity; dilatancy; synchrotron imaging; semi-solid deformation

1. Introduction

The drive to improve fuel economy and reduce CO₂ emissions continues to incentivise the development of low-cost lightweight high-strength cast alloys for automotive and other transport applications ^[1]. These light alloys are required to possess excellent strength and fatigue properties, together with good weldability and machinability, all at a low cost ^{[1][2]}.

35 These properties are heavily influenced by the presence of the microstructural features and
36 solidification defects like hot tear ^{[3][4]}, segregation ^{[5][6][7]}, and porosity ^{[8][9]}, which exist in
37 forms of (a) gas porosity ^[10], (b) shrinkage porosity ^[11], and shrinkage bands in twin-roll and
38 High pressure die castings (HPDC) ^[12]. The nucleation of these solidification defects can be
39 traced to the semi-solid state having relatively high solid fractions during the solidification. It
40 is known that at these higher solid fractions, a network of solid is formed and as a consequence,
41 the permeability of the mushy zone will decrease, resulting in difficulty in further feeding of
42 the liquid. Based on the amount of fractions of solid, the solid network has been interpreted as
43 a continuous solid skeleton ^{[13][14]} and cohesion-less granular solid ^{[15][16][17]}. The thermo-
44 mechanical response of this network under deformation is understood to play a key role in the
45 formation of defects.

46 Laboratory and synchrotron-based semi-solid deformation tests have been extensively carried
47 out by researchers to understand the thermo-mechanical behaviour of several aluminium alloys,
48 particularly binary Al-Cu alloys ^[18]. While tensile tests have been conducted to determine the
49 strength and ductility of the network ^[19], shear ^[20] and compression tests ^[18] were used to study
50 the rheology of the semi-solid. Tzimas et al. ^[18] reported semi-solid compression tests of Al-4
51 wt.% Cu alloys that cover the effect of solid fraction, strain rate and grain morphology and
52 identified different factors affecting the flow resistance ^[18]. Kim et al. ^[21], Kang et al. ^[22], and
53 Kapranos et al. ^[23] conducted compression experiments to study the rheological behaviour of
54 various aluminium alloys at different solid fractions and strain rates and reported liquid
55 segregation and cracks at the edge of the specimens. The development of advanced synchrotron
56 experimentation via fast X-ray techniques have allowed observations of the microstructural
57 features during deformation *in situ* ^{[24][25]}. Kareh et al. ^[26], and Cai et al. ^[27] reported *in situ*
58 compression experiments and quantified the granular motion and dilatancy at various imposed
59 strains. The *in situ* studies confirmed the role of volume dilation during tensile and compressive
60 deformation of the semi-solid in forming defects such as hot tears and shear bands ^[20]. Several
61 theories of micro-mechanisms of hot tear defect formation have been proposed and criteria for
62 cracking have been developed based on the experimental studies. ^{[28][29]}. However, most of
63 these models do not account for the local thermal history, formation of combined gas and
64 shrinkage porosity, and its effect on the initiation of hot cracks. Since the shrinkage and gas
65 porosity are believed to account for about 35% of the total defects in high pressure die cast
66 components ^[30], a 3D, real-time information of the defect formation is critical to develop

67 predictive models for porosity and cracks at both microscopic (size and shape) and macroscopic
68 (location and volume fraction) levels.

69 The diffusion driven growth of the gas micro-porosity based on the differential solubility of
70 hydrogen in the melt and the solid is well-known in the literature ^[31] ^[32] ^[33]. Early research on
71 gas porosity was focused on the quenching experiments and post-mortem observation of the
72 microstructures. Lee and Hunt ^[31] were the first to report the observation of porosity in Al-Cu
73 alloys in real-time using an X-ray temperature gradient stage, and the quantification of the
74 cooling rate on the pore radius and the volume fractions. Subsequently, experimental studies
75 on the hydrogen micro-porosity during directional solidification were reported by Arnberg and
76 Mathiessen ^[32], Liao et al. ^[33], and Lie et al. ^[34]. Catalina et al. ^[35] observed the change in pore
77 shape to ellipsoid when the pore is surrounded by the solutal layer ahead of the solid-liquid
78 interface and estimated the increase in growth rate during engulfment. Based on the X-ray
79 radiographic observations, several empirical models of pore growth, which account for the
80 influence of hydrogen diffusion, volumetric shrinkage ^[36] and presence of microstructural
81 features like intermetallics ^[37], have been reported. Likewise, the formation of shrinkage
82 porosity due to lack of feeding has been reported via several experimental studies. For e.g.,
83 Gourlay et al. ^{[16][20]} investigated the mechanism for the formation of shrinkage bands and Li
84 et al. ^[38] reported the influence of melt flow and externally solidified crystals on the formation
85 of defect bands in HPDC of AZ91D magnesium alloy.

86 However, the mechanisms of pore growth during deformation and purely convective
87 conditions, and the role of liquid flow in promoting porosity growth are neither reported nor
88 quantified, to the best of our knowledge. This information is critical to understand and develop
89 models to predict the size and location of porosity. In this study, compression of semi-solid Al-
90 Si-Cu die-cast alloys, with and without modified copper content, has been performed to
91 quantify the flow-driven pore nucleation and growth. The liquid fraction distribution and the
92 nucleated porosity in the dilatant bands were quantified at different strain values during
93 compression. A 1D diffusion-controlled gas porosity model was used to quantify the flux
94 required for pore growth, which provided insights into the propensity of advective hydrogen
95 transport in enhancing the growth of hydrogen pores. In what follows, we present the
96 experimental methodology, analysis and quantification of the 4D (3D+time) data
97 characterising the nature of deformation-induced and solidification-driven pore growth.

98

99 2. Materials and Methods

100 Die-cast aluminium alloy ADC12 and a Modified ADC12 alloy (will be termed as MADC12
101 henceforth) with an additional 10 wt.% copper were used in the study. The modified alloy was
102 used to achieve an enhanced contrast between the primary phase and the inter-dendritic liquid.
103 A secondary objective of modifying the alloy was to investigate the influence of the change in
104 freezing range on hydrogen pore growth, and thus the propensity of cracking. The chemical
105 composition of the major alloying elements (Table 1) was assessed using inductively-coupled
106 plasma atomic emission spectroscopy (ICP-AES) technique.

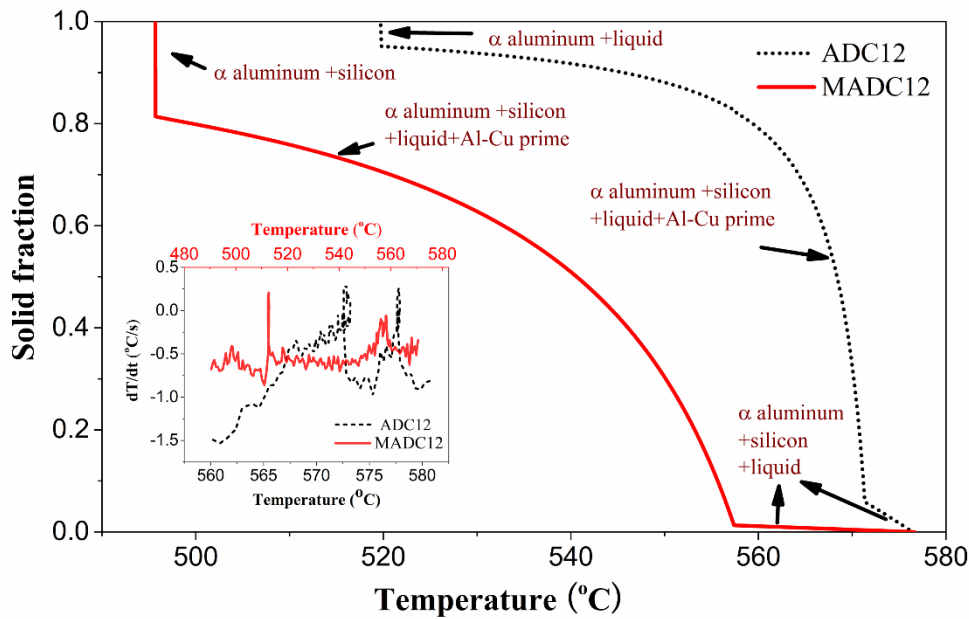
107 **Table I: Chemical assay of the alloys under study**

Sample	Cu (wt.%)	Fe (wt.%)	Si (wt.%)
ADC12	1.82	0.74	11.9
Modified ADC12	10.43	0.80	10.5

108

109 2.1 Sample preparation

110 Calculated amounts of ADC12 alloy and 99.99% copper were melted in a coreless induction
111 furnace fitted with a pure graphite crucible lined with magnesite refractory. The molten alloy
112 was continuously stirred for 2 minutes with a graphite rod to ensure that the alloy composition
113 is uniform. Then the metal was poured into a cast iron die of dimension $250 \times 50 \times 40 \text{ mm}^3$
114 and allowed to cool in air. The ADC12 and MADC12 alloy ingots were then machined into 3
115 mm diameter cylinders using wire electro discharge machining. The length of the final samples
116 was $5.4 \pm 0.3 \text{ mm}$. The Scheil solidification model in Thermo-Calc® [39] was used to obtain the
117 freezing range for determining the experimental conditions, and is shown in figure 1. The
118 estimation of solidification range by Thermo-Calc® were validated by conducting bulk
119 cooling experiments as shown in inset of figure 1. Since ADC12 has a larger freezing range,
120 the hot-cracking propensity is expected to be higher.

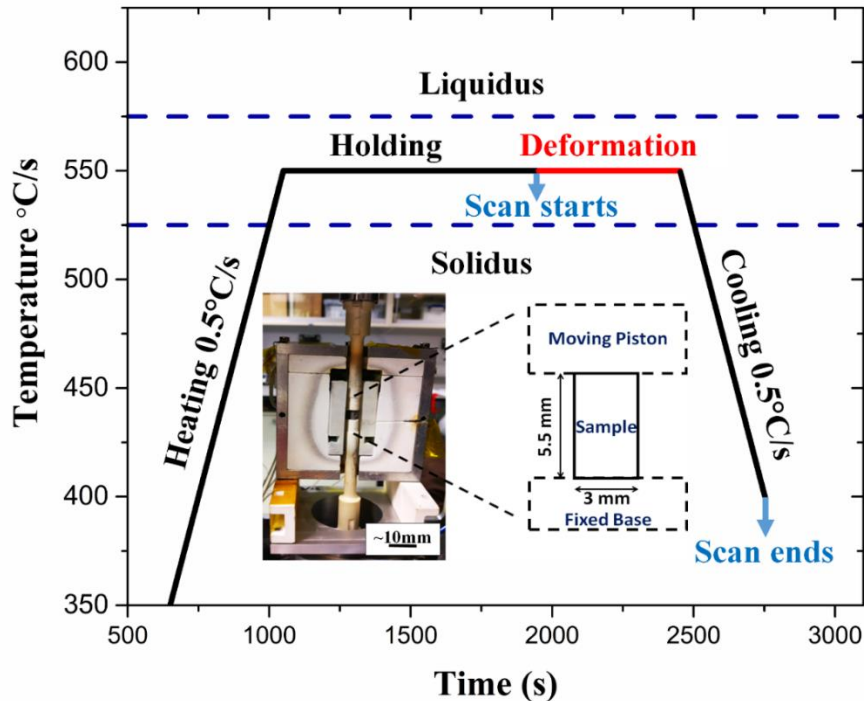


121

122 Fig. 1—Solid fraction vs. temperature for MADC12 and ADC12 alloys, calculated using the
 123 Thermo-Calc® Scheil solidification module. The inset shows the cooling rates of the bulk
 124 samples being cooled at 0.5 °C/s, with the lower X-axis indicating the temperatures for
 125 ADC12 alloy and the upper X-axis for MADC12 alloy.

126 **2.2 Semi-solid compression experiments**

127 The semi-solid compression experiments were conducted at I12 beamline of the Diamond
 128 Light Source ^[40] (beamtime reference - EE16188). A PID-controlled resistance furnace fitted
 129 with an X-ray transparent window is mounted on a custom-made mechanical rig for the semi-
 130 solid compression experiments. Details of the setup can be found in ^{[27][41]}. The mechanical
 131 rig used was specifically designed to conduct *in situ* deformation and has high precision loading
 132 control (as low as 100 nm/s) and force measurement (least count 0.1 N). A schematic of the
 133 experimental set-up is shown in figure 2. The specimen was placed at the centre of alumina
 134 shackles as shown in the figure 2. A preload of approximately 7 N was applied to hold the
 135 sample in place during compression experiments. The loading ram was adjusted to maintain
 136 the preload during the experiment to account for thermal expansion during heating. The thermal
 137 cycle followed during the experimentation along with the sample arrangement are presented in
 138 figure 2. A loading rate of 5 μm/s and the solid fraction of 75%±5% were maintained during
 139 the compression experiments. The fraction of solid was determined by the temperature from
 140 Scheil modelling as well as from the *in situ* images.



141

142 Fig. 2—Thermal cycle followed during the semi-solid compression test. The inset shows the
 143 sample mounted inside the furnace.

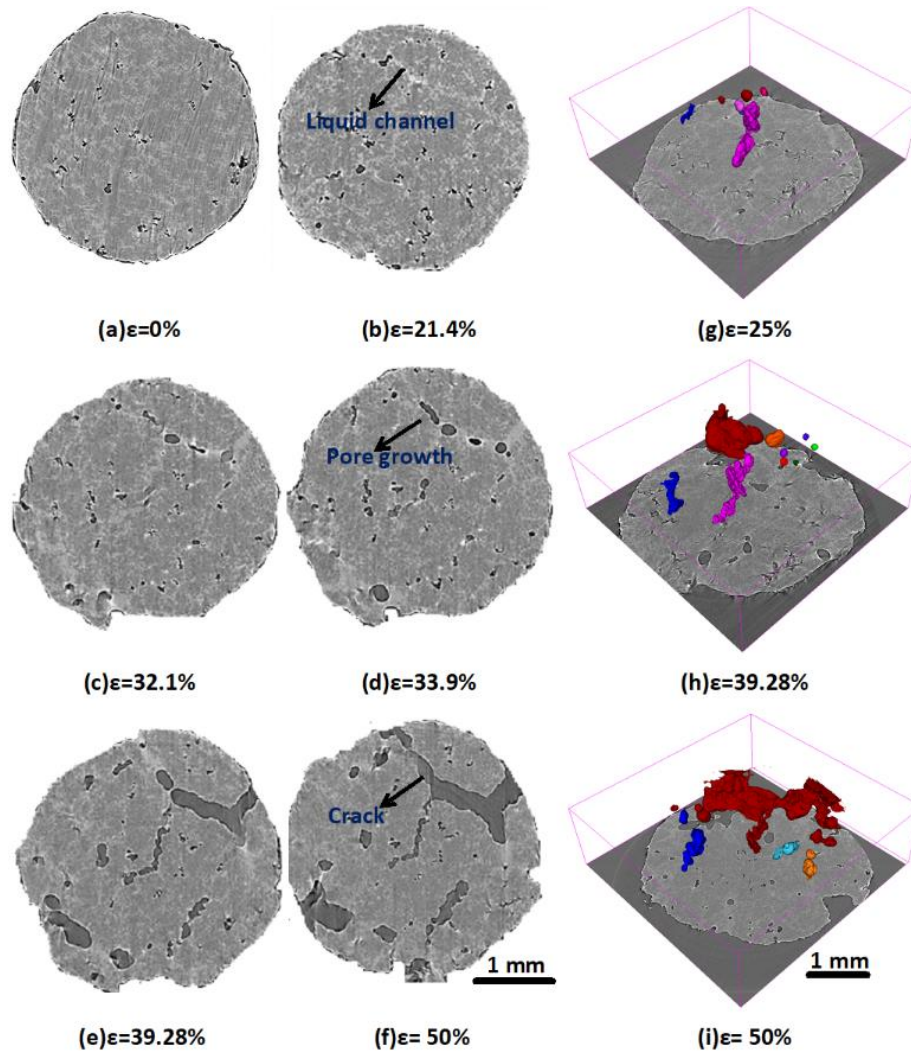
144 **2.3 Data acquisition and image processing**

145 A monochromatic X-ray beam with an energy of 53 keV was used in the experiment. During
 146 the deformation, a set of 38 tomograms were acquired using a PCO.Edge camera coupled with
 147 I12's camera module 3, which corresponds to a field of view of 8 mm × 6 mm ^[40]. A total of
 148 600 projections were taken for every 180° rotation of the sample for each tomogram, obtaining
 149 a voxel size of 3.2 μm. The exposure time was 32 ms per projection, with the total time of each
 150 scan being 19.2 s. Each scan was taken continuously without any additional sample rotation,
 151 which allowed for the continuous data collection. The 3D scan was reconstructed using filtered
 152 back-projection to produce an 1885 × 1885 × 2149 voxel volume. The image was filtered using
 153 anisotropic and 3D median filters to remove noises. The filtered image was segmented using
 154 trainable weka segmentation plugin ^[42] in Fiji ImageJ ^[43], which makes use of machine learning
 155 tools.

156 **3. Results and Discussions**

157 The transverse slices of the MADC12 sample at an approximate height of 600 μm from the
 158 bottom slice and at 6 different strain values are shown in figure 3 (a-f). In the figure, the dark
 159 grey represents the porosity and the lighter grey indicates the inter-dendritic liquid, while the
 160 intermediate grey colour corresponds to the primary solid phase. The longitudinal strain values

161 indicated were measured by dividing the instantaneous length of the sample by the initial
 162 length. The sequence of the mechanisms leading to the formation of a crack is described as
 163 follows.



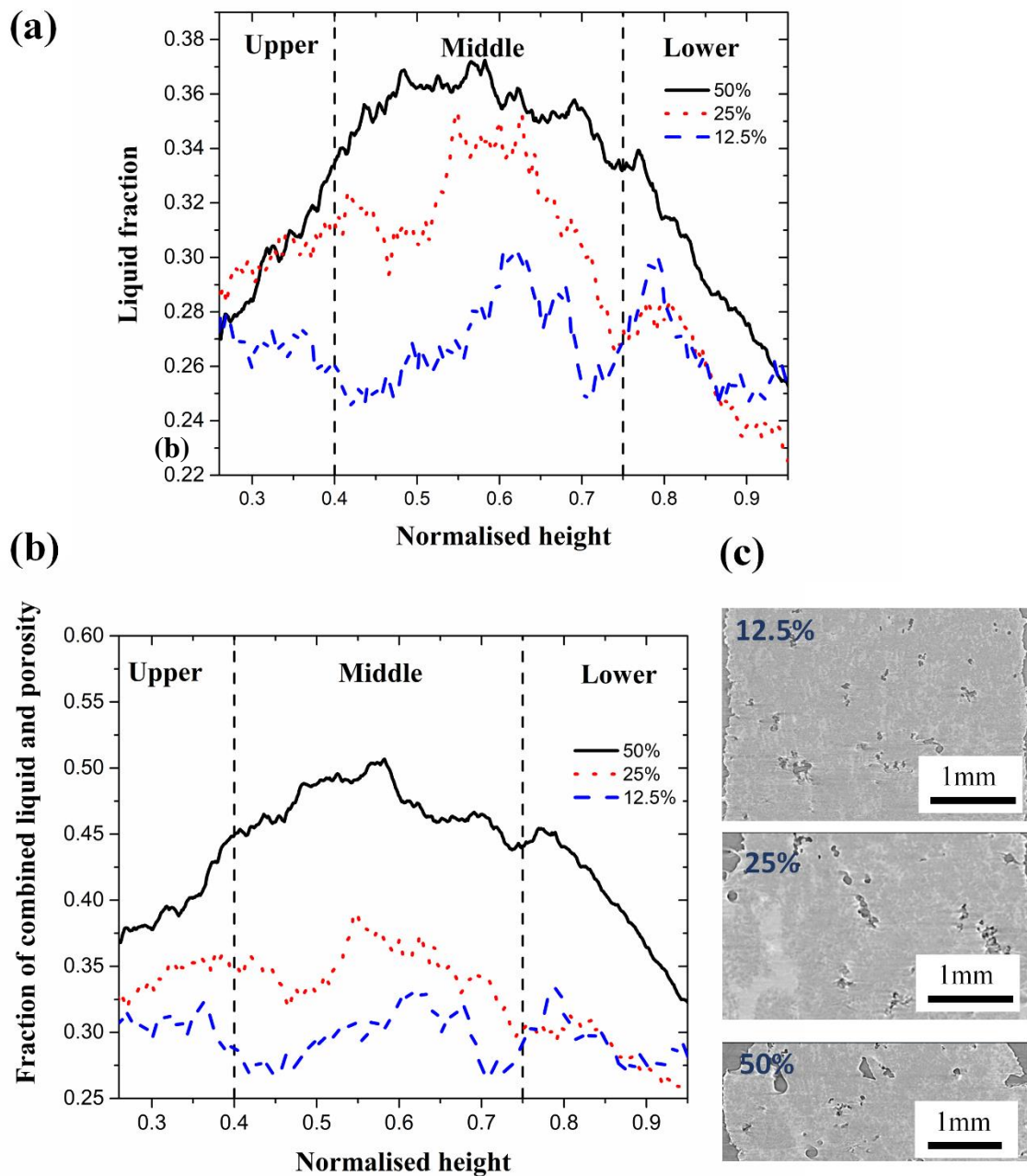
164

165 Fig. 3— (a-f) Transverse slices of the MADC12 sample (75% fraction solid) at a height of
 166 $\sim 600 \mu\text{m}$ from the sample bottom at different strains, showing the formation and growth of
 167 gas porosity and the subsequent development of a hot tear (g-i) 3D rendered images at
 168 equivalent time instances, with each colour representing a contiguous segment of porosity.

169 3.1.1 Formation of liquid channels

170 The inter-dendritic liquid, which was distributed uniformly ($\sim 25 \pm 5\%$) (figure 3(a)) before the
 171 compression commenced, formed several isolated liquid channels on the application of
 172 compression load (one such channel at $\epsilon=21.4\%$ is marked in figure 3(b)). The measured values
 173 of liquid fraction at different strains along the loading axis (figure 4(a)), which shows the
 174 localization of liquid channels in the middle of sample. Note that the height of sample for each

175 area liquid fraction was normalized with respect the total height of the sample at that instant of
 176 deformation. The increase in the fraction is due to the increased area at the middle of the sample
 177 coupled with the development of liquid channels due to dilatancy. These liquid pockets were
 178 later observed to be the location of nucleation of gas micro-porosity during deformation as well
 179 as the cooling stages.



180
 181 Fig. 4—Development of the (a) liquid and (b) combined liquid and pore fraction along the
 182 loading axis at different strain values. (c) Longitudinal slices at different strain values
 183 showing the pore and liquid channel growth

184 **3.1.2 Pore nucleation, growth and coalescence**

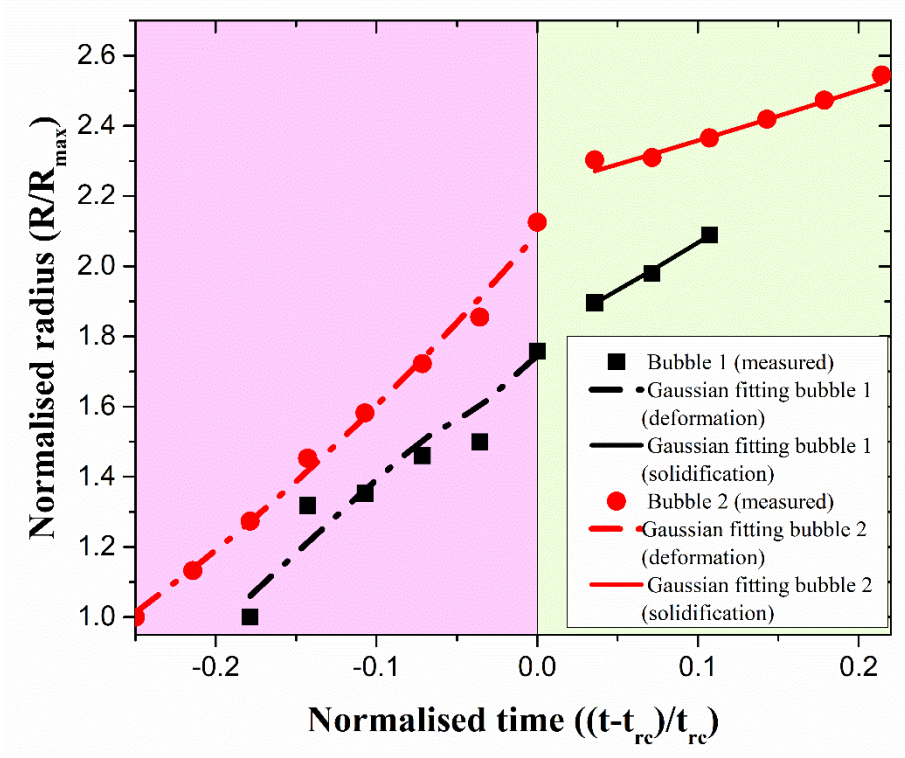
185 The nucleation of new gas pores was observed in the liquid channels at various strain values
186 throughout the deformation stage (figure 3(b)). The pores grew consistently while the mush
187 deformed with expanding liquid channels. Plausibly, the feeding of the liquid resulted in a
188 convective influx of hydrogen into the liquid pockets, thereby increasing the overall local
189 hydrogen concentration. This is hypothesized based on the observation that the pores were
190 predominantly spherical during the deformation regime, indicating a diffusion-controlled gas
191 pore growth. Furthermore, a secondary influence on pore growth was the pressure drop in the
192 dilatant bands, which can also lead to pore volume dilation. The pores retained spherical shape
193 until they encountered a solid (figure 3d). The phenomenon was also observed and reported by
194 Cai et al.,^[27] who had defined different stages of dilatancy controlled shrinkage growth, which
195 eventually led to cracking. The values of combined area of liquid fraction and porosity at
196 different strains along the loading axis were determined and shown in figure 4(b). By
197 comparing figure 4(a) and 4(b) it is clear, that the pore growth due to volume dilation picks up
198 after 25% strain and most of these voids were concentrated around the middle of the sample.
199 Longitudinal slices shown in figure 4(c), shows the ‘middle’ region indicated in the figure 4(a)
200 and (b), in which the localization of liquid channel and voids can be seen. It should be noted
201 that, in earlier studies by Stefanescu^[44] and Khalajzadeh^[45], a shrinkage induced flow term,
202 introduced and its role on shrinkage growth had been discussed. This flow term is analogous
203 to the dilatancy induced flow discussed in this study.

204

205 **3.2 Regimes of gas porosity growth: (a) deformation and (b) solidification**

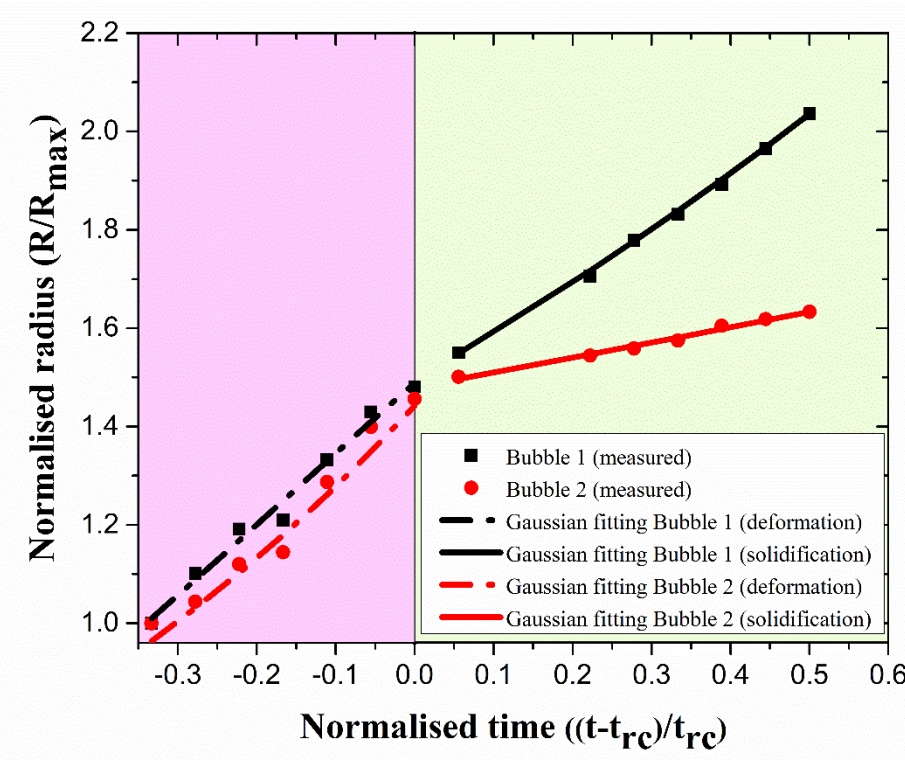
206 The gas pores which did not coalesce and grew independently during both deformation and
207 solidification stages were tracked from the tomograms obtained from the *in situ* experiments.
208 The radius of these isolated pores at various strain values were measured, normalised and data
209 of 2 typical pores are represented in figures 5 for the MADC12 alloy. The details of
210 normalising is provided in Supplementary material-1 (refer to the electronic supplementary
211 material). It is evident that the growth behaviour of the pores altered noticeably at the end of
212 the deformation (when the cooling initiated). Based on the experimental observations, two
213 regimes of pore growth were defined, namely, (a) deformation induced and (b) solidification
214 controlled.

215



216

217 Fig. 5—Evolution of the gas micro-porosity with time during deformation and cooling
 218 (solidification) stages for MADC12 alloy. Here R_{max} and t_{rc} represents the maximum radius
 219 (end of solidification) and time instant at which the regime changes respectively



220

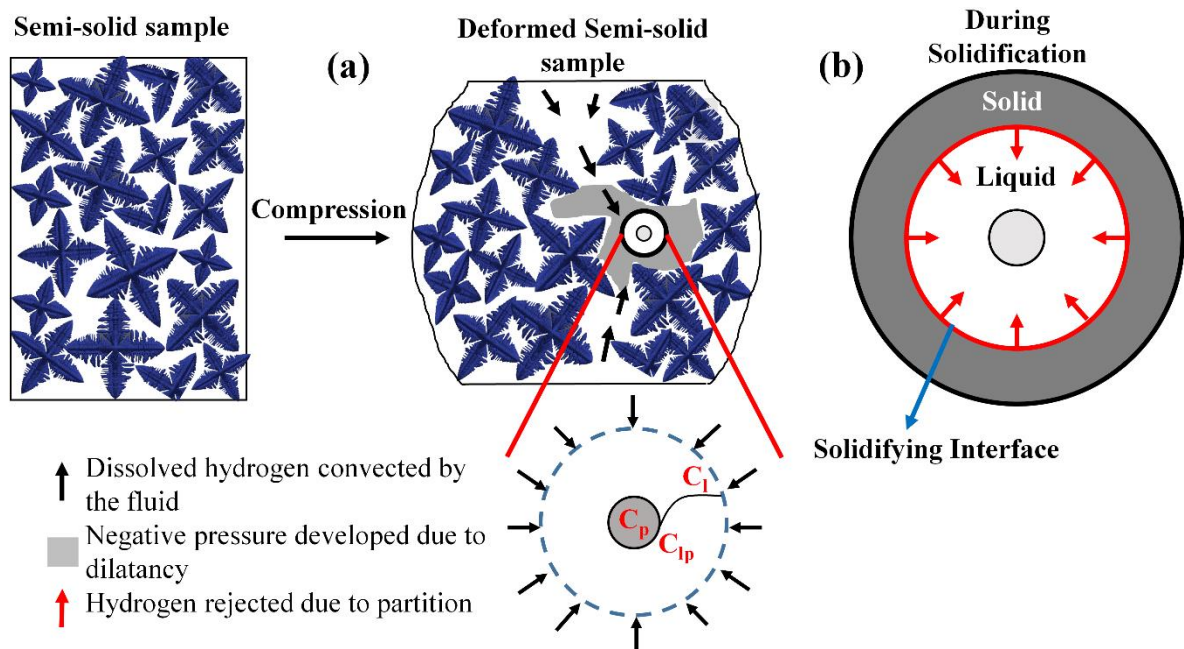
221 Fig. 6—Evolution of gas micro-porosity with time during deformation and cooling
 222 (solidification) stages for ADC12 alloy.

223 Recently, Sun et al., modelled the diffusion-controlled gas pore growth in aluminium melt
 224 using a Gaussian distribution function [37]. Following their work, the pore growth in two
 225 regimes of the present data was fit using a Gaussian distribution function as given in equation
 226 1.

$$227 \quad r = \frac{A}{t_{SD} \times \sqrt{2\pi}} \times \exp\left(-2 \frac{(t - t_{mean})^2}{t_{SD}^2}\right) \quad [1]$$

228 where, A is a constant corresponding to the amplitude of the Gaussian distribution, and t_{mean}
 229 and t_{SD} are mean and standard deviation of the Gaussian function. The fitted curves are shown
 230 with the experimental observations in figures 5 and 6 and the adjusted R^2 value indicate a
 231 reasonably good fit.

232 The proposed hypothesis of a combined deformation and solidification-driven hydrogen micro-
 233 porosity is represented schematically in figure 7. The regions within the circles essentially
 234 show a representative elementary volume (REV) surrounding a gas pore. Figure 7(a) shows the
 235 deformation-driven flow of the liquid, which fed the hydrogen into the pore by convective
 236 transport, while 7(b) shows the rejection of hydrogen during the solidification of neighbouring
 237 solid structures.



238
 239 Fig. 7— Schematic of the proposed pore growth mechanism during (a) deformation and (b)
 240 solidification. The black arrows in (a) represents the liquid flow associated with dilatancy.

241 The black arrows in (a) and red arrows in (b) represent hydrogen flux into the representative
242 volume around a gas pore.

243 3.3. Numerical evaluation of advective hydrogen influx

244 Since the isolated pores show a distinct growth behaviour during deformation as compared to
245 solidification, an understanding of amount of hydrogen influx carried by the liquid would be
246 useful in correlating the flow-induced growth under different processing environments such as
247 twin roll casting, HPDC etc. A calculation of 1D diffusion-driven hydrogen gas pore growth
248 was performed using a numerical model discussed in [46]. It was assumed that a constant value
249 of hydrogen concentration existed at the boundary of the domain (figure 7), which represents
250 the amount of hydrogen brought in by the inter-dendritic flow. Using the pore growth model,
251 the necessary hydrogen concentration at the boundary that resulted in an equivalent growth
252 obtained from the experiments was determined. Note that this analysis only accounts for the
253 growth of the spherical pore under the influence of increased hydrogen influx due to liquid
254 flow.

255 A pre-existing hydrogen gas pore of radius R in liquid supersaturated with hydrogen was
256 considered, which grows instantaneously due to diffusion of hydrogen into the pore. The size
257 of the REV (with radius R_{domain}) was assumed to be larger compared to the diffusion boundary
258 layer. By balancing the rate of mass increase inside the pore, the influx of concentration at
259 boundary, and the flow due to the movement of the boundary itself, the growth rate of the
260 liquid-pore interface is evaluated as follows:

$$261 \quad V_{int} = \frac{1}{(C_p - C_{lp} - C_d)} D_l \frac{\partial C_l}{\partial r} \quad [2]$$

262 where C_b , C_p , C_{lp} , C_d , are the hydrogen concentration (in cc/100 g of Al) in the far field, inside
263 the pore, at the interface and an additional term arising due to the liquid-pore interface
264 movement respectively, and are functions of the pore radius and reference pressure (details in
265 supplementary information 2). The details of the individual terms are given in supplementary
266 information 2. D_l is the mass diffusivity of hydrogen in aluminium. In this study, for the
267 calculation of C_p and C_{lp} the reference pressure for the liquid was set at 1 atm. The surface
268 tension and the mass diffusivity values were taken from Sasikumar et al [47] and Lee et al [31].
269 [46]. The equivalent radius, measured from the tomographic scans, was assumed to be the initial
270 radius of the sample. A fixed concentration input at the far-field liquid that drives the influx of
271 hydrogen can be obtained as follows:

$$C_l = C_{lp} + \frac{V_{\text{int}}(C_p - C_{lp} - C_d)}{D_l} R \quad [3]$$

Using the above relation, a concentration change created by the deformation-induced flow was estimated and is reported for a few pore radii in Table 2. The model was used to calculate the input concentration for a range of input radii (12.47-36.01 μm for MADC12 and 69.95-131.74 μm for ADC12) and the corresponding rate of change of the concentration at the REV interface was calculated and found to be of the order $\sim 10^{-5}$.

Table II: The concentration input at domain boundary estimated from the model

Alloy	Radius of the gas pore (μm) in the two regimes			Avg. concentration input (cc/100g Al) between two scans	
	Pore	Deformation	Solidification	Deformation	Solidification
MADC12	1	29.8	68.8	2.6×10^{-4}	1.9×10^{-5}
	2	37.9	70.4	6.3×10^{-4}	1.5×10^{-5}
ADC12	1	69.9	119.3	8.0×10^{-4}	1.1×10^{-4}
	2	77.0	124.5	4.8×10^{-4}	5.2×10^{-5}

Using mass conservation, this rate of change of concentration at the interface is related to the convective flux given by the equation 4. Note that we have assumed that the velocity of the liquid flow is of the same order as the deformation rate (V)

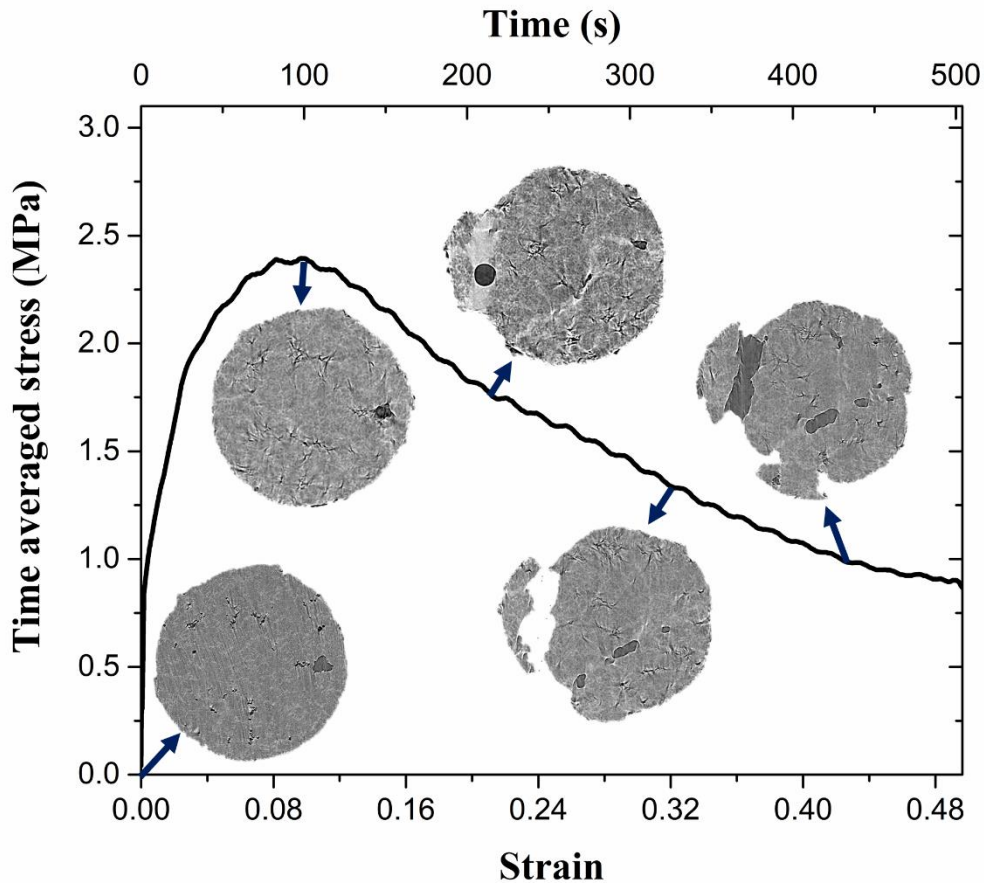
$$\frac{\partial C}{\partial t} = V \frac{\partial C}{\partial x} \quad [4]$$

It can be seen that by increasing the velocity of deformation, the concentration build-up at REV increases, for a given far-field concentration. This increase in the concentration gradient between the REV boundary and the pore-liquid interface drives the pore growth. This information is helpful in evaluating flow-driven hydrogen concentration build-up and eventual porosity, particularly for high-pressure die casting environments, where flow rates are very high ($\sim 20\text{-}60$ m/s) [2].

3. Stress-strain behaviour during compression

The occurrence of dilatancy is ascertained with the help of flow stress vs. strain data obtained from the experiment. The normalised stress vs. strain curve with the insets in the figure indicating the transverse slice at every 10% strain from the semi-solid compression is shown in the figure 8. Note that the stress is calculated as the ratio of the applied load to the initial sample area. The graph shows characteristic peak at a strain value of ~ 0.1 which indicated that the stress developed due to the pinning of the grains was being relieved by the development of

297 liquid channels due to dilatancy (inset at 20% strain). Further dilatation of the liquid channel and
298 nucleation and growth of porosity resulted in a continuous decrease of the load, and eventual
299 formation of a hot-tear at around 0.32 strain.



300

301 Fig. 8—Stress-Strain curve for MADC12 alloy. Insets display the transverse slice of the
302 specimen at the indicated strain values in the range of 0-50%.

303 **Conclusions:**

304 Ultrafast synchrotron X-ray imaging was utilized to observe the porosity growth in 2 different
305 Al-Si-Cu die-cast alloy specimens at $\sim 75 \pm 5\%$ solid fraction during compression and
306 solidification conditions. In the present work, we have proposed, a mechanism of flow-driven
307 hydrogen pore growth which is critical for predicting final porosity in high-pressure die-cast
308 components. The following conclusions were drawn from the study.

- 309 1. Two distinct regimes of hydrogen pore growth, namely deformation-induced flow driven
310 growth and solidification controlled growth were observed and quantified. The growth rates
311 were determined by measuring the equivalent pore radius from *in situ* experiments. The
312 measured growth rate values showed a clear and abrupt change at the end of deformation

313 regime, and were also found to agree with the trends reported in the literature using
314 Gaussian distribution functions.

315 2. The role of dilatancy in deformation induced pore growth via advective hydrogen transport
316 was ascertained using quantification of localized liquid channels and the stress-strain
317 behaviour of the semi-solid under compressive loading.

318 3. The hydrogen concentration influx during deformation induced flow that closely represents
319 the observed experimental trend was estimated using a 1D diffusion model. This revealed
320 a hydrogen concentration boundary condition, and can be further used to correlate flow-
321 driven hydrogen influx for different processing routes.

322

323 **Acknowledgements:**

324 The authors thank the University Research Program at Ford Motor Company, USA for partial
325 financial support. We are grateful to Diamond light source for the beamtime (EE16188-1), Dr.
326 Sara Nonni, Dr. Nolwenn Legall and Sebastian Marucci for their help during beamtime. S.K
327 and P.D.L acknowledge the sanction of the project P1299 under the SPARC (Scheme for
328 Promotion of Academic and Research Collaboration) initiative. B.C. acknowledges the support
329 provided by the Diamond Birmingham Collaboration and Alan Turing Fellowship. The support
330 from the ferrous metallurgy and the machine tools laboratories at IIT Bombay in preparing the
331 samples is acknowledged.

332 **References**

- 333 1 P.K.M. Jason, Rowe: *Advanced Materials in Automotive Engineering*, 1st edn.,
334 Woodhead Publishing Limited, 2012.
- 335 2 S.H. Huo, M. Qian, G.B. Schaffer, and E. Crossin: *Fundamentals of Aluminium*
336 *Metallurgy*, 2011.
- 337 3 D.G. Eskin, Suyitno, and L. Katgerman: *Prog. Mater. Sci.*, 2004, vol. 49, pp. 629–711.
- 338 4 C. Puncreobutr, P.D. Lee, K.M. Kareh, T. Connolley, J.L. Fife, and A.B. Phillion: *Acta*
339 *Mater.*, 2014, vol. 68, pp. 42–51.
- 340 5 C.M. Gourlay, A.K. Dahle, and H.I. Laukli: *Metall. Mater. Trans. A*, 2004, vol. 35, pp.
341 2881–91.
- 342 6 P. Rousset, M. Rappaz, and B. Hannart: *Metall. Mater. Trans. A*, 1995, vol. 26, pp.
343 2349–58.
- 344 7 N. Shevchenko, S. Boden, G. Gerbeth, and S. Eckert: *Metall. Mater. Trans. A Phys.*
345 *Metall. Mater. Sci.*, 2013, vol. 44, pp. 3797–808.

- 346 8 P.D. Lee and J.D. Hunt: *Acta Mater.*, 2001, vol. 49, pp. 1383–98.
- 347 9 R.C. Atwood, S. Sridhar, W. Zhang, and P.D. Lee: *Acta Mater.*, 2000, vol. 48, pp.
348 405–17.
- 349 10 S.G. Lee, A.M. Gokhale, G.R. Patel, and M. Evans: *Mater. Sci. Eng. A*, 2006, vol. 427,
350 pp. 99–111.
- 351 11 S.G. Lee and A.M. Gokhale: *Scr. Mater.*, 2006, vol. 55, pp. 387–90.
- 352 12 X. Li, S.M. Xiong, and Z. Guo: *Mater. Sci. Eng. A*, 2015, vol. 633, pp. 35–41.
- 353 13 G. Lesoult, C.A. Gandin, and N.T. Niane: *Acta Mater.*, 2003, vol. 51, pp. 5263–83.
- 354 14 A. Zavaliangos: *Int. J. Mech. Sci.*, 1998, vol. 40, pp. 1029–41.
- 355 15 C.M. Gourlay, H.I. Laukli, and A.K. Dahle: *Metall. Mater. Trans. A*, 2007, vol. 38, pp.
356 11–6.
- 357 16 K.M. Kareh, C. O’Sullivan, T. Nagira, H. Yasuda, and C.M. Gourlay: *Acta Mater.*,
358 2017, vol. 125, pp. 187–95.
- 359 17 M. Sistaninia, S. Terzi, A.B. Phillion, J.M. Drezet, and M. Rappaz: *Acta Mater.*, 2013,
360 vol. 61, pp. 3831–41.
- 361 18 E. Tzimas and A. Zavaliangos: *Acta Mater.*, 1999, vol. 47, pp. 517–28.
- 362 19 S. Terzi, L. Salvo, M. Suéry, N. Limodin, J. Adrien, E. Maire, Y. Pannier, M. Bornert,
363 D. Bernard, M. Felberbaum, M. Rappaz, and E. Boller: *Scr. Mater.*, 2009, vol. 61, pp.
364 449–52.
- 365 20 C.M. Gourlay and a K. Dahle: *Nature*, 2007, vol. 445, pp. 70–3.
- 366 21 W.Y. Kim, C.G. Kang, and B.M. Kim: *J. Mater. Process. Technol.*, 2007, vol. 191, pp.
367 372–6.
- 368 22 C.G. Kang, J.S. Choi, and K.H. Kim: *J. Mater. Process. Technol.*, 1999, vol. 88, pp.
369 159–68.
- 370 23 P. Kapranos, T.Y. Liu, H. V. Atkinson, and D.H. Kirkwood: *J. Mater. Process.*
371 *Technol.*, 2001, vol. 111, pp. 31–6.
- 372 24 S. Karagadde, P.D. Lee, B. Cai, J.L. Fife, M.A. Azeem, K.M. Kareh, C. Puncreobutr,
373 D. Tsioulas, T. Connolley, and R.C. Atwood: *Nat. Commun.*, 2015, vol. 6, p. 8300.
- 374 25 E. Guo, A.B. Phillion, B. Cai, S. Shuai, D. Kazantsev, T. Jing, and P.D. Lee: *Acta*
375 *Mater.*, 2017, vol. 123, pp. 373–82.
- 376 26 K.M. Kareh, P.D. Lee, R.C. Atwood, T. Connolley, and C.M. Gourlay: *Nat Commun*,
377 2014, vol. 5, p. 4464.
- 378 27 B. Cai, S. Karagadde, L. Yuan, T.J. Marrow, T. Connolley, and P.D. Lee: *Acta Mater.*,
379 2014, vol. 76, pp. 371–80.
- 380 28 M. Rappaz, J.M. Drezet, and M. Gremaud: *Metall. Mater. Trans. A Phys. Metall.*
381 *Mater. Sci.*, 1999, vol. 30, pp. 449–55.

- 382 29 M. Sistaninia, A.B. Phillion, J.M. Drezet, and M. Rappaz: *Metall. Mater. Trans. A*
383 *Phys. Metall. Mater. Sci.*, 2011, vol. 42, pp. 239–48.
- 384 30 F. Bonollo, N. Gramegna, and G. Timelli: *Jom*, 2015, vol. 67, pp. 901–8.
- 385 31 P.D. Lee and J.D. Hunt: *Acta Mater.*, 1997, vol. 45, pp. 4155–69.
- 386 32 R.H. Mathiesen, L. Arnberg, F. Mo, T. Weitkamp, and A. Snigirev: *Phys. Rev. Lett.*,
387 1999, vol. 83, pp. 5062–5.
- 388 33 H. Liao, W. Song, Q. Wang, L. Zhao, and R. Fan: *Jom*, 2012, vol. 64, pp. 22–7.
- 389 34 L. Zhao LieHengcheng: *China Foundry*, 2011, vol. 8, pp. 14–8.
- 390 35 A. V. Catalina, D.M. Stefanescu, S. Sen, and W.F. Kaukler: *Metall. Mater. Trans. A*
391 *Phys. Metall. Mater. Sci.*, 2004, vol. 35 A, pp. 1525–38.
- 392 36 H. Yin and J.N. Koster: *Isij Int.*, 2000, vol. 40, pp. 364–72.
- 393 37 S. Sun, Q. Hu, W. Lu, Z. Ding, M. Xia, and J. Li: *Metall. Mater. Trans. A Phys.*
394 *Metall. Mater. Sci.*, 2018, vol. 49, pp. 4429–34.
- 395 38 X. Li, Z. Guo, and S. Xiong: *Mater. Charact.*, 2017, vol. 129, pp. 344–52.
- 396 39 B.S. Andersson, Thomas Helander, Lars Hdghmd, Pingfang Shi: *Calphad Comput.*
397 *Coupling Phase Diagrams Thermochem.*, 2002, vol. 26, pp. 273–312.
- 398 40 M. Drakopoulos, T. Connolley, C. Reinhard, R. Atwood, O. Magdysyuk, N. Vo, M.
399 Hart, L. Connor, B. Humphreys, G. Howell, S. Davies, T. Hill, G. Wilkin, U.
400 Pedersen, A. Foster, N. De Maio, M. Basham, F. Yuan, and K. Wanelik: *J.*
401 *Synchrotron Radiat.*, 2015, vol. 22, pp. 828–38.
- 402 41 B. Cai, P.D. Lee, S. Karagadde, T.J. Marrow, and T. Connolley: *Acta Mater.*, 2016,
403 vol. 105, pp. 338–46.
- 404 42 I. Arganda-Carreras, V. Kaynig, C. Rueden, K.W. Eliceiri, J. Schindelin, A. Cardona,
405 and H.S. Seung: *Bioinformatics*, 2017, vol. 33, pp. 2424–6.
- 406 43 J. Schindelin, I. Arganda-Carreras, E. Frise, V. Kaynig, M. Longair, T. Pietzsch, S.
407 Preibisch, C. Rueden, S. Saalfeld, B. Schmid, J.Y. Tinevez, D.J. White, V.
408 Hartenstein, K. Eliceiri, P. Tomancak, and A. Cardona: *Nat. Methods*, 2012, vol. 9, pp.
409 676–82.
- 410 44 D.M. Stefanescu and A. V Catalina: *Int. J. Cast Met. Res.*, 2011, vol. 24, pp. 144–50.
- 411 45 V. Khalajzadeh, K.D. Carlson, D.G. Backman, and C. Beckermann: *Metall. Mater.*
412 *Trans. A Phys. Metall. Mater. Sci.*, 2017, vol. 48, pp. 1797–816.
- 413 46 S. Karagadde and P. Dutta: *Int. Commun. Heat Mass Transf.*, 2016, vol. 79, pp. 16–20.
- 414 47 R. Sasikumar, M.J. Walker, S. Savithri, and S. Sundarraj: *Model. Simul. Mater. Sci.*
415 *Eng.*, DOI:10.1088/0965-0393/16/3/035009.

416

417

418 **Figure Captions**

419 Fig. 1—Solid fraction vs. temperature for MADC12 and ADC12 alloys, calculated using the
420 Thermo-Calc® Scheil solidification module. The inset shows the cooling curves of the bulk
421 samples being cooled at 0.5 °C/s, with the lower X-axis indicating the temperatures for ADC12
422 alloy and the upper X-axis for MADC12 alloy.

423

424 Fig. 2—Thermal cycle followed during the semi-solid compression test. The inset shows the
425 sample mounted inside the furnace.

426

427 Fig. 3— (a-f) Transverse slices of the MADC12 sample (75% fraction solid) at a height of
428 ~600 µm from the sample bottom at different strains, showing the formation and growth of gas
429 porosity and the subsequent development of a hot tear (g-i) 3D rendered images at equivalent
430 time instances, with each colour representing a contiguous segment of porosity.

431

432 Fig. 4—Development of the (a) liquid and (b) combined liquid and pore fraction along the
433 loading axis at different strain values. (c) Longitudinal slices at different strain values showing
434 the pore and liquid channel growth

435

436 Fig. 5—Evolution of the gas micro-porosity with time during deformation and cooling
437 (solidification) stages for MADC12 alloy. Here R_{max} and t_{rc} represents the maximum radius
438 (end of solidification) and time instant at which the regime changes respectively

439

440 Fig. 6—Evolution of gas micro-porosity with time during deformation and cooling
441 (solidification) stages for ADC12 alloy.

442

443 Fig. 7— Schematic of the proposed pore growth mechanism during (a) deformation and (b)
444 solidification. The black arrows in (a) represents the liquid flow associated with dilatancy. The
445 black arrows in (a) and red arrows in (b) represent hydrogen flux into the representative volume
446 around a gas pore.

447

448 Fig. 8—Stress-Strain curve for MADC12 alloy. Insets display the transverse slice of the
449 specimen at the indicated strain values in the range of 0-50%.